atmosphere

MDPI

Article

Case Study of Mesoscale Precipitation Areas within the Comma Head of an Extratropical Cyclone

Yu Zhao [1,*], Xin Lan [1,2], Shuling Li [3] and Chengfang Yang [4]

[1] Key Laboratory of Meteorological Disaster, Ministry of Education (KLME)/Joint International Research Laboratory of Climate and Environment Change (ILCEC)/Collaborative Innovation Center on Forecast and Evaluation of Meteorological Disasters (CIC-FEMD), Nanjing University of Information Science & Technology, Nanjing 210044, China; lxnuist@163.com
[2] Sanya Meteorological Bureau, Sanya 572000, China
[3] Harbin Meteorological Bureau, Harbin 150028, China; lishuling1968@163.com
[4] Shandong Provincial Meteorological Observatory, Jinan 250031, China; cf_yang70@hotmail.com
* Correspondence: yuzhao@nuist.edu.cn

Abstract: On 12–13 February 2016, a record-breaking rain–snow event during the passage of an extratropical cyclone occurred in Shandong Province, China, in which the 24 h precipitation totals at 48 of 123 national meteorological stations in Shandong Province broke their historical records for the month of February, and a further 25 stations recorded their second-largest February totals. This paper investigates the evolution of the mesoscale precipitation areas and the mechanisms responsible for the formation, organization, and maintenance of the mesoscale precipitation areas, using FY-2G satellite data, Doppler radar observations, and a Weather Research and Forecasting (WRF) model numerical simulation at 4 km grid spacing. The main results show that the comma head cloud of the cyclone developed from four echo strips. Intense precipitation was related to the mesoscale elongated precipitation areas (EPAs) of reflectivity >30 dBZ within the stratiform clouds. The formation and development of the EPAs coincided with the activities of a low-level shear line and an associated increase in frontogenesis. The simulated EPAs occurred in an environment of conditional instability (CI), inertial instability (II), and conditional symmetric instability (CSI). In the initial stage of the elongated rainfall areas (ERAs), rainfall was initiated by the frontal forcing in the presence of elevated CI, and II was generated by upright convection. During the development stage of the ERAs, the CI was absent, and condensational heating was enhanced. II occurred in the absence of upright convection, and it seems likely that the presence of II is a diabatic signature of the precipitation itself. Upper-level II intensified the convective systems by enhancing outflow aloft, and II caused the ERAs to organize. Thus, II played an important role in the organization and maintenance of the ERAs. The frontogenesis provided the dynamic condition for the release of the instability. Enhanced CSI and II intensified slantwise convection, and combining with enhanced frontogenesis, intensified the ERAs. The echo, ascent, and frontogenesis in snowfall areas were weaker than those in rainfall areas.

Keywords: extratropical cyclone; rain–snow event; comma head; instability; frontogenesis

Citation: Zhao, Y.; Lan, X.; Li, S.; Yang, C. Case Study of Mesoscale Precipitation Areas within the Comma Head of an Extratropical Cyclone. *Atmosphere* **2022**, *13*, 942. https://doi.org/10.3390/atmos13060942

Academic Editors: Yu Du, Xiang Ni and Xiaofei Li

Received: 4 May 2022
Accepted: 6 June 2022
Published: 9 June 2022

1. Introduction

On 12–13 February 2016, an extratropical cyclone generated in southern Anhui Province and moved northeastward into the East China Sea (Figure 1), causing two major precipitation bands: a northeast–southwest-oriented precipitation band extending from northern Jiangsu to northern Hubei Province associated with a surface cold front, and a west–east-oriented precipitation band over Shandong Province related to a surface warm front (Figure 2a). An average 24 h precipitation amount of 24.6 mm was observed over Shandong Province, with maximum precipitation of 55.9 mm in Zicuan (Figure 2a). A transition from rain to sleet and then the snow was observed in northern and central Shandong Province. The daily precipitation at 48 of 123 national meteorological stations in Shandong Province

broke their historical records for the month of February, and a further 25 recorded their second-highest February totals.

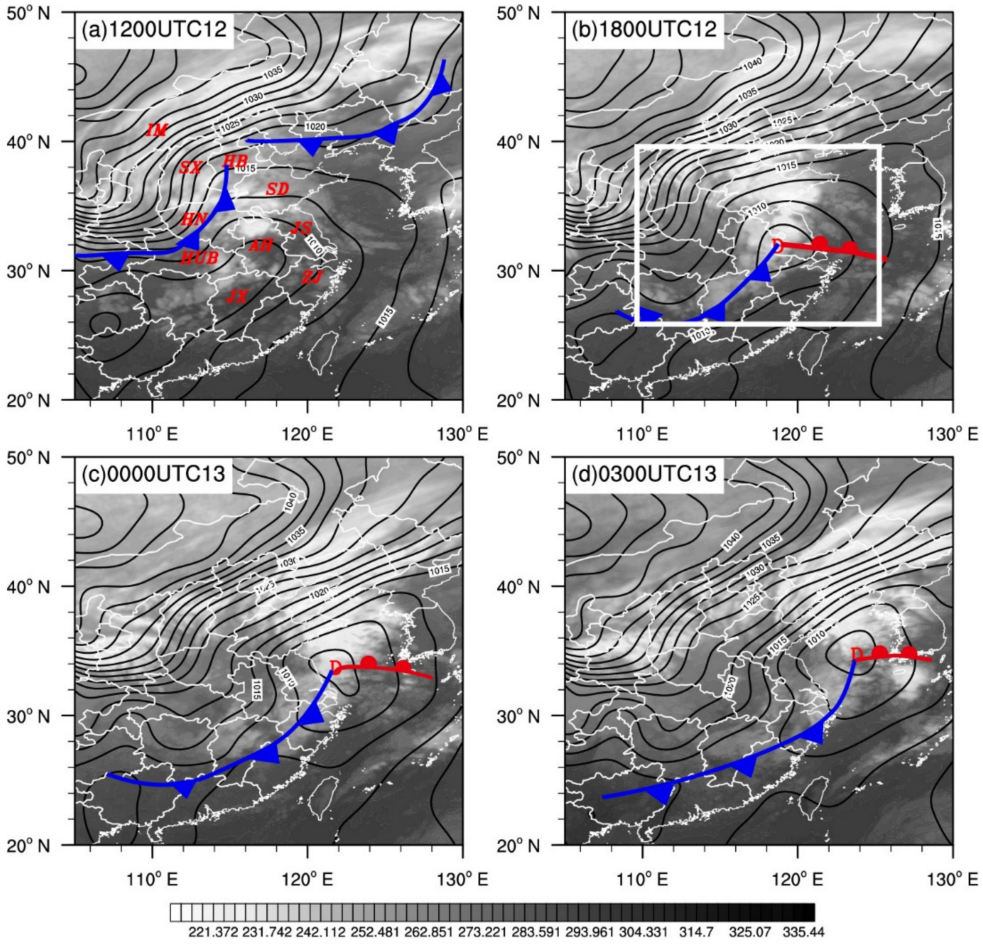

Figure 1. Infrared satellite images from FY-2G at (**a**) 1200 UTC 12 February, (**b**) 1800 UTC 12 February, (**c**) 0000 UTC 13 February, and (**d**) 0300 UTC 13 February 2016. Overlaid on the images are the surface low-pressure center (D), cold front (blue line with triangles), warm front (red line with semicircles) as well as the sea level pressure field (black lines; unit: hPa). The locations of Shandong (SD), Anhui (AH), Jiangsu (JS), Hebei (HB), Henan (HN), Shanxi (SX), Zhejiang (ZJ), Jiangxi (JX), and Hubei (HUB) Provinces are labeled in (**a**).

This extreme rain–snow event in Shandong Province was produced by the mesoscale precipitation areas within the comma head of the extratropical cyclone [1]. Cyclones originating over the Yangtze–Huaihe River Basin (which are referred to as Jianghuai cyclones in China) are an important synoptic system responsible for snowstorms over northern China during the cold season. Two pathways of Jianghuai cyclones are observed: eastward-moving cyclones that deepen weakly and move into the East China Sea after generation and whose comma-head cloud mainly affects North China and Shandong Province [2,3], and northeastward-moving cyclones that deepen significantly after generation and produce a wide range of rain or snow over northeastern China [4,5]. Some investigations on snowstorms associated with Jianghuai cyclones, such as their circulation patterns [6–8], physical variables [9–11], dry- and cold-air activities [12], and mesoscale gravity waves [13,14], have been carried out. Additionally, the airstreams and cloud features have been reported by Zhao et al. [15–17].

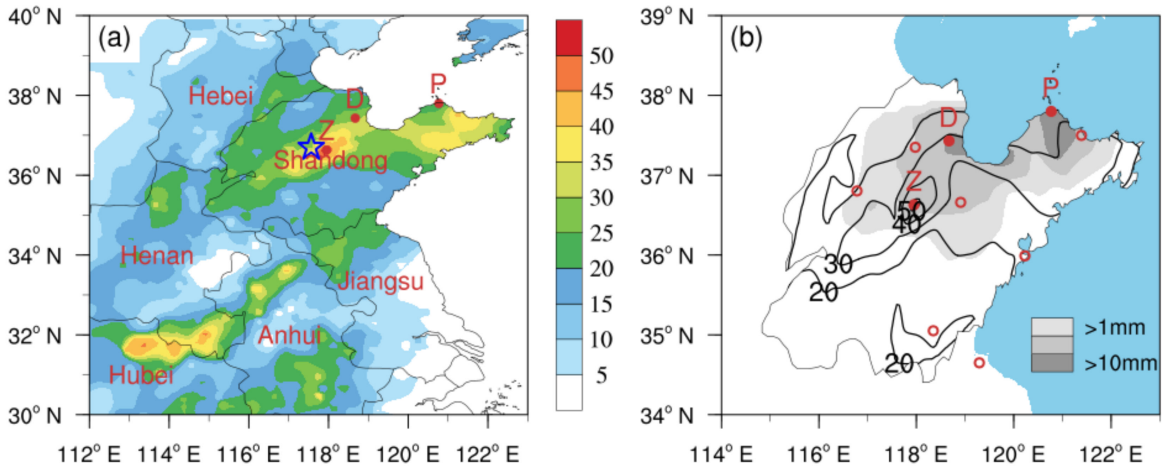

Figure 2. Rain gauge observed (**a**) precipitation and (**b**) snowfall (unit: mm) from 1200 UTC 12 to 1200 UTC 13 February 2016. The locations of Shandong, Anhui, Jiangsu, Hebei, Hubei, and Henan Provinces are labeled in (**a**). The letters "Z", "D", and "P" denote the cities of Zichuan, Dongying, and Penglai, respectively. The blue star in (**a**) indicate Zhangqiu sounding station. Red open circles in (**b**) denote the locations of Doppler radars used in radar mosaic.

Intense snow in Europe and the United States is mostly associated with extratropical cyclones, and so many related studies have been well documented [18–24]. These snowstorms are mainly distributed in the comma-head portion of a developing cyclone. The northwest quadrant of a mature cyclone usually exhibits a warm occluded front structure [25,26], where a juxtaposition of dry and moist airstreams can decrease the moist symmetry stability [27]. In a climatological study of banded precipitation in the northeast United States, Novak et al. [18] found that a single-banded structure is the most common band type and is responsible for the intense local precipitation in the comma-head portion of developing cyclones. Such a band structure significantly influences the intensity, timing, and cumulative precipitation. The synoptic and mesoscale circulation may affect the formation of mesoscale snow bands. However, the mesoscale precipitation bands resulting from frontal circulation have presented a challenge to human forecasters [27,28]. So, studying the structural and dynamic evolution of mesoscale snow bands can improve the skill of cold-season quantitative precipitation forecasting (QPF).

Conditional symmetric instability (CSI) has been proposed as a possible explanation for banded precipitation [29]. Emanuel [30] and Xu [31] revealed the relationship between symmetry stability and frontogenetical forcing from theory and showed that intense single bands could form via a coupled relationship between frontogenesis and symmetric instability. Case studies and climatological analyses show that intense precipitation bands in the northeast United States are related to strong frontogenesis, weak moisture symmetric stability, and sufficient moisture [32–35]. Weisman [36] pointed out that snowfall occurred in the early stage of a cyclone, and weak conditional instability (CI) was beneficial to the organization of the snow bands.

Convective instability and symmetric instability do not exist in isolation and can coexist. They play important roles together [37–39] and can transform each other [40]. Holt and Thorpe [41] proposed that upright convection can create inertial instability (II) within the frontal zone via the vertical advection of low-momentum air. The ensuing slantwise convection response was termed "delta-M adjustment" [42], and the delta-M adjustment is regarded as a mechanism leading to the mutual transformation of convective instability and symmetric instability [41,43,44].

Although the CSI and dynamical forcing are important in band formation, the stability and mesoscale forcing vary in different stages of snowfall. For example, in a case study of a snowstorm over the United States, Novak et al. [45] demonstrated the evolutions of II, CSI, CI, and moisture in different stages of a snow band. Studies by Schultz et al. [46]

and Schumacher et al. [47] showed that dry symmetric instability, CI, and II in convective precipitation bands develop in unsaturated synoptic and mesoscale environments. Novak et al. [19], in a statistical and composite analysis of intense precipitation within the comma head of extratropical cyclones, investigated the variation in lower-tropospheric frontogenesis and conditional stability over intense snow bands prior to their formation, maturity, and dissipation. They found that lower-tropospheric frontogenesis nearly doubles, and the conditional stability above the frontal zone reduces during the 6 h prior to snow band formation.

CSI and CI have also been documented in snowstorms associated with eastward-moving Jianghuai cyclones [48,49]. However, such cyclones differ in some respects compared with cyclones in Europe and America. Investigation into the structural and dynamic evolution of the mesoscale precipitation areas of such cyclones is scarce, and related understanding is limited, which leads to low QPF skill associated with Jianghuai cyclones, and thereby large forecast deviations in terms of precipitation intensity, position, timing, and so on.

Motivated by the above context, this paper examines the structural and dynamic evolution of mesoscale precipitation areas with the aid of Weather Research and Forecasting (WRF) model simulation, thereby providing a reference for the forecasting of precipitation associated with Jianghuai cyclones. Answers to the following three specific questions will be sought: (1) What are the cloud features of the comma head of the Jianhuai cyclone? (2) What are the stability and forcing mechanisms responsible for the formation and development of the mesoscale precipitation areas? (3) What are the differences in the structure between rainfall and snowfall?

Section 2 describes the data, model configuration, and calculations used in this study. An overview of the precipitation, synoptic-scale environmental conditions, and evolution of the mesoscale precipitation areas are introduced in Section 3. Verification of the numerical experiment is described in Section 4. Section 5 examines the evolution of stability and frontogenesis during the formation and development stages of the mesoscale elongated precipitation areas (EPAs). Finally, a summary and discussion are presented in Section 6.

2. Data and Methods

2.1. Observational Data

Data from the FY-2G satellite, which is China's third operational geostationary meteorological satellite, are used to investigate the evolution of the cyclone's clouds. The Stretched Visible and Infrared Spin Scan Radiometer on board FY-2G includes four infrared channels (IR1, IR2, IR3, and IR4) and one visible channel, with 5 km and 1.25 km resolutions at nadir, respectively. The infrared brightness temperature in the spectral range of 10.3–11.3 μm (IR1) with 1 h intervals is used in this study. To further investigate the evolution of the precipitation areas, Doppler weather radar observations at Jinan, Weifang, Binzhou, Yantai, Qingdao, Linyi, and Lianyungang (red open circles shown in Figure 2b) are used. These radars are S-band, with a wavelength of 10 cm, operating in volume coverage pattern 21 (VCP21), and scanned at nine elevation angles of 0.5°, 1.5°, 2.4°, 3.4°, 4.3°, 6.0°, 9.9°, 14.6°, and 19.5° with a volumetric update time of 6 min during this event. Real-time analysis data of the Global Forecast System (GFS) of the National Centers for Environmental Prediction (NCEP), with a 6 h interval and 0.25° × 0.25° horizontal resolution (available online at https://rda.ucar.edu/datasets/ds084.1/, accessed on 15 April 2021) are used to investigate the environmental conditions of the precipitation event.

2.2. Model Configuration

The model simulation of the extreme rain–snow event was run using triple-nested grids of (36, 12, and 4 km) in version 3.7 of the WRF model [50] with 50 sigma levels. 36, 12, and 4 km domains had (x, y) dimensions of 202 × 146, 283 × 271, and 319 × 328, respectively. The 12 km nested domain covered the region across which the Jianghuai cyclone moved, and the 4 km nested (one-way) domain was centered on the precipitation center over

Shandong Province. The full model physics was used, including the WSM3 microphysical scheme, RRTM longwave, and Dudhia shortwave radiation schemes, the Monin–Obukhov (Janjic) surface layer and Mellor–Yamada–Janjic TKE scheme for planetary boundary layer processes, and a unified Noah land surface scheme [51]. The Kain-Fritsch [52] cumulus parameterization was used on the 36 and 12 km domains, and no cumulus parameterization was used on the 4 km domain. The model was initialized at 0600 UTC on 12 February and integrated for 30 h, ending at 1200 UTC on 13 February. GFS real-time analysis data at a resolution of 0.25° × 0.25° were used to initialize the model and lateral boundary conditions at 6 h intervals. The outputs of 36, 12, and 4 km was 3 h, 1 h, and 1 h, respectively.

2.3. Calculations

Following Novak et al. [45], moist symmetric stability is examined by using the saturation equivalent potential vorticity (EPV), which is defined as

$$\mathrm{EPV} = g\eta \cdot \nabla \theta_{es} \tag{1}$$

where g is the acceleration of gravity, η is the three-dimensional absolute vorticity vector, and θ_{es} denotes saturation equivalent potential temperature. The full wind was used in calculating the EPV. When the slope of the θ_{es} surface is steeper than that of the absolute momentum (M) surface or EPV < 0, CSI is present.

Following Miller [53], the simplified 2D form of frontogenesis was used to analyze the frontal forcing:

$$F_{2D} = \frac{1}{|\nabla\theta|}\left[-\frac{\partial\theta}{\partial x}\left(\frac{\partial u}{\partial x}\frac{\partial\theta}{\partial x}+\frac{\partial v}{\partial x}\frac{\partial\theta}{\partial y}\right)-\frac{\partial\theta}{\partial y}\left(\frac{\partial u}{\partial y}\frac{\partial\theta}{\partial x}+\frac{\partial v}{\partial y}\frac{\partial\theta}{\partial y}\right)\right] \tag{2}$$

where θ denotes potential temperature, u and v represent horizontal wind, and the full wind was used in calculating the frontogenesis.

3. Observational Analysis

3.1. Overview of Precipitation

Rainfall first started in southern Shandong Province at around 0900 UTC on 12 February 2016 and then extended northward to the whole of Shandong Province by 2100 UTC on 12 February. By 2300 UTC on 12 February, a transition from rain to snow in northern and central Shandong Province was observed, and the precipitation persisted until 1000 UTC on 13 February, with a record 24 h accumulated precipitation of 55.9 mm in Zicuan and 52 mm in Boshan (Figure 2a). The distribution of 24 h accumulated snowfall exhibits a narrowed snow region over northern Shandong Province, with six rain gauge observations exceeding 10 mm, and a maximum snowfall of 14 mm in Penglai (Figure 2b). According to the change in the phase of precipitation, the event can be divided into two periods. First, rainfall maintained from 0900 UTC to 2300 UTC on 12 February, which is defined as the rainfall period. After that, the rain changed into snow in northern and central Shandong Province, while other places sustained rain during the period from 2300 UTC 12 to 1000 UTC on 13 February, which is defined as the snowfall period.

3.2. Synoptic Condition

The extreme precipitation event occurred under favorable atmospheric conditions. From 0000 UTC to 1200 UTC on 12 February, a 500 hPa longwave trough embedded within a cold vortex (a synoptic-scale low pressure with a cold core in the middle and upper troposphere) remained over Mongolia and western China (Figure 3a,b), with an apparent frontal zone ahead of the trough, keeping the cold air moving southward continually. South of 40° N, two shortwave troughs merged and moved to the west of Shandong Province (Figure 3a,b), providing an ascent that favored cyclogenesis and precipitation. Two 200 hPa jets were present: a primarily zonal jet across southern China and a south-westerly jet over northeastern China (Figure 3a). Shandong Province was located on the right side of the

entrance region of the south-westerly jet and the left side of the exit region of the zonal jet at 1200 UTC on 12 February, where strong divergence existed (Figure 3b). Below the 500 hPa trough was a vortex with a west–east-oriented shear line at 850 hPa (Figure 3c). During the night, the vortex moved northeastward, with the shear line intensifying and moving northward to central Shandong by 1800 UTC on 12 February, and the low-level jet south of the vortex substantially intensified (Figure 3c,d), transporting abundant warm and moist air to Shandong Province. As shown in the distribution of the temperature advection at 850 hPa, the warm advection over Shandong Province evidently intensified during the 6 h period (Figure 3c,d). Below these low-level jets, a northeast–southwest-oriented surface inverted trough was observed in eastern China, and a cold front was located to the west of this surface inverted trough (Figure 1a). A 1005 hPa cyclone was formed over southern Anhui Province at 1800 UTC on 12 February (Figure 1b). By 0000 UTC on 13 February, the cyclone had moved into the East China Sea, with the minimum central pressure decreasing to 1002.5 hPa (Figure 1c), and a transition from rain to snow in northern and central Shandong was observed because of the decrease in temperature.

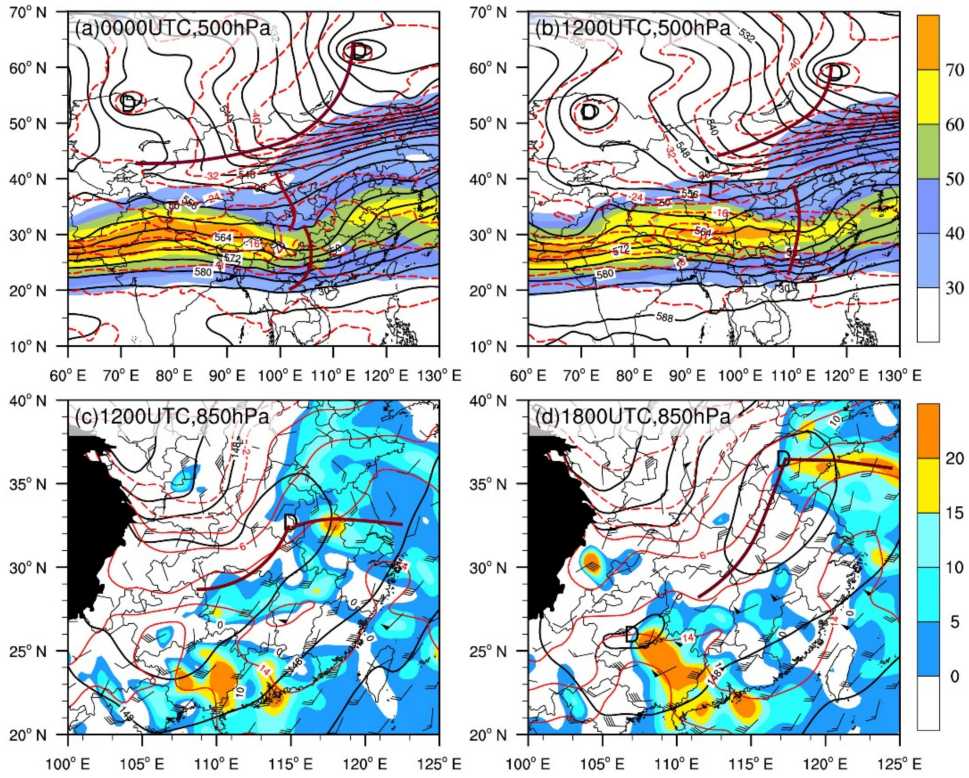

Figure 3. NCEP GFS analysis at (**a**) 0000 UTC, (**b**,**c**) 1200 UTC, and (**d**) 1800 UTC on 12 February 2016. (**a**,**b**) Geopotential height (black solid lines; unit: dagpm), temperature (red dashed lines; unit: °C) at 500 hPa, and 200 hPa wind speeds $\geq$ 30 m·s^{-1} are shown shaded. The brown thick lines denote troughs. (**c**,**d**) Geopotential height (black solid lines; unit: dagpm), temperature (red lines; unit: °C), wind barbs (full barb = 4 m·s^{-1}, pennant = 20 m·s^{-1}), and temperature advection >0 (shaded; unit: 10^{-5} K·s^{-1}) at 850 hPa. The brown thick lines denote shear lines.

3.3. Clouds of the Cyclone

The FY2-G infrared satellite cloud images show the evolution of the Jianghuai cyclone's clouds (Figure 1). At 1200UTC on 12 February, a baroclinic leaf cloud over central and eastern Inner Mongolia was associated with the cold front, while clouds over the border of Henan and Shanxi and southern Shandong were linked with the vortex and associated shear line (Figure 1a). The shear line clouds developed into a comma cloud pattern with a comma head and tail (denoted by the white square in Figure 1b), which did not connect with the northern baroclinic leaf cloud (Figure 1b). At 0000 UTC on 13 February, the comma

head of the cyclone developed obviously and grew in coverage, and it was connected with the baroclinic leaf cloud to the north (Figure 1c). The cyclone moved eastward over the sea, and the comma head of the cyclone mainly affected Shandong peninsular by 0300 UTC on 13 February (Figure 1d). Thus, the precipitation in Shandong Province was produced by a low-level vortex and associated shear line prior to the formation of the cyclone, while these phenomena were responsible for the comma head after the formation of the cyclone.

3.4. Mesoscale Features of the Precipitation Clouds

Mosaic radar reflectivity data at high resolution (0.01° × 0.01°) were used to understand the mesoscale features of the precipitation clouds. The convection was initiated in the evening (i.e., 0900UTC on 12 February) and then organized into a comma cloud pattern consisting of numerous mesoscale precipitation regions of reflectivity > 30 dBZ during its life span. The major precipitation areas of interest in Figure 4 were traced from the reflectivity data at 6 min intervals and are labeled sequentially based on the times they first appeared.

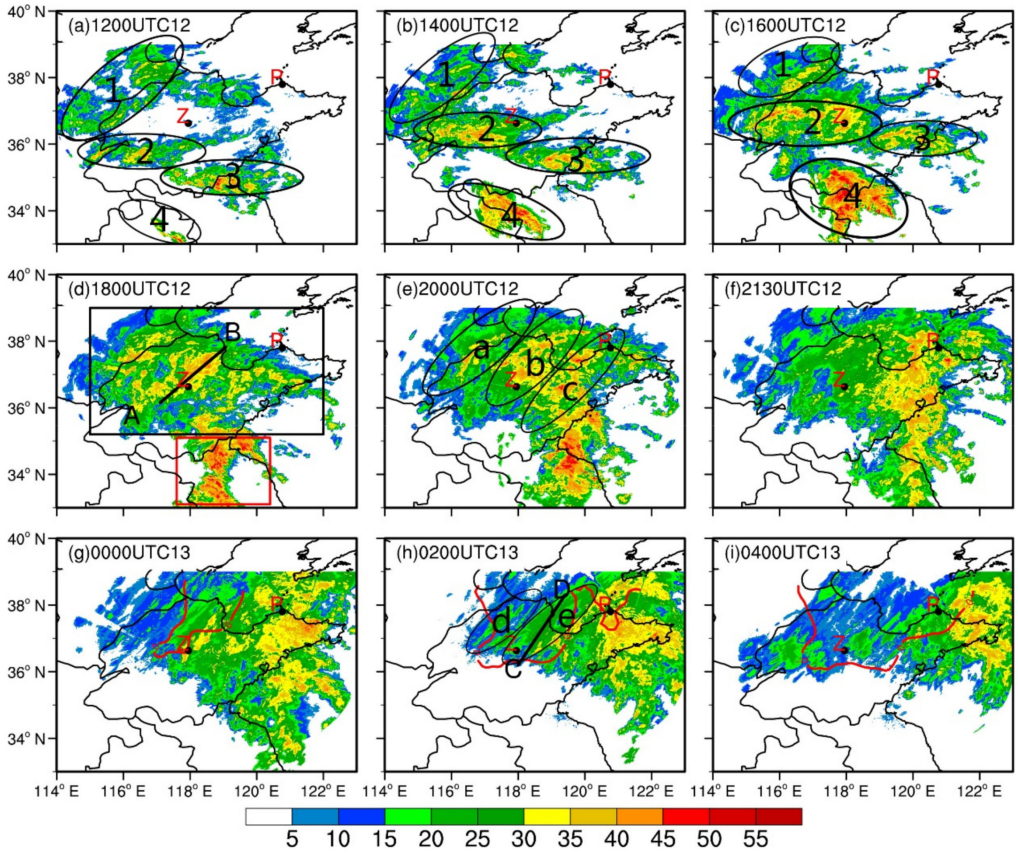

Figure 4. Radar composite reflectivity (unit: dBZ) derived from the mosaic radar reflectivity at (**a**) 1200 UTC 12, (**b**) 1400 UTC 12, (**c**) 1600 UTC 12, (**d**) 1800 UTC 12, (**e**) 2000 UTC 12, (**f**) 21,300 UTC 12, (**g**) 0000 UTC 13, (**h**) 0200 UTC 13, and (**i**) 0400 UTC 13 February 2016. The black rectangular box in (**d**) denotes the position of the comma head of the cyclone, while the red rectangular box in (**d**) denotes the tail of the comma cloud of the cyclone. The numbers 1 to 4 inside ellipses in (**a**–**c**) are used to trace the evolution of the major echoes. The letters a to e inside ellipses in (**e**,**h**) are used to trace the mesoscale rainfall areas or snowfall areas. The red contours in (**g**–**i**) represent 0 °C isotherms from the surface meteorological station. The black dots above the letters Z and P denote the cities of Zichuan and Penglai, respectively.

Figure 4a shows three echo strips in Shandong Province at 1200 UTC on 12 February: the first along the Hebei–Shandong border region, with weak echoes but more extensive coverage (labeled "1"); the second over southwestern Shandong (labeled "2"); and the third

along the border region of Shandong and Jiangsu with stronger echoes (labeled "3"). These echo strips were mainly composed of stratiform clouds and a small number of cumulus clouds with reflectivity > 35 dBZ. Additionally, a northwest–southeast-oriented convective cloud echo strip (labeled "4") was developing in northeastern Anhui. These echo strips occurred in a region of intense low-level wind convergence associated with the shear line (Figure 3c). Two hours later, these echo strips developed and grew in coverage, especially echo strip 4, which intensified significantly (Figure 4b). By 1600 UTC on 12 February, accompanied by the movement of the shear line, these echo strips propagated northward and joined, with parts of echo strip 4 moving into southeastern Shandong (Figure 4c). Although the surface cyclone had formed by 1500 UTC on 12 February, no echo areas existed over southeastern Shandong (Figure 4c), implying that the comma cloud pattern did not form completely.

At 1800UTC on 12 February, the above four echo strips developed into a whole body, forming a complete comma cloud pattern, with the tail of the comma cloud not completely included owing to the coverage of the figure. The comma head (denoted by the black rectangle in Figure 4d), corresponding to the warm front clouds, had a wide coverage, among which cumulus clouds grew in coverage and extended in a northeast–southwest orientation to form numerous mesoscale elongated rainfall areas (ERAs), with the maximum radar reflectivity being > 50 dBZ over central Shandong, contributing to the intensification of hourly rainfall rate. The mesoscale ERAs were categorized nonbanded rather than well-defined single-banded precipitation bands [18,19]. The tail of the comma cloud (indicated by the red rectangle box in Figure 4d) was narrow and mainly composed of cumulus clouds, corresponding to the cold front clouds.

The Jianghuai cyclone developed into its mature stage at 2000 UTC on 12 February, when strong reflectivity within the comma head began to exhibit the features of vortex echoes (Figure 4e). Among them, the convective elements began to extend along a northeast–southwest orientation, forming the mesoscale ERAs a, b, and c (black circle shown in Figure 4e). The rainfall rate of 9.8 mmh^{-1} in Zichuan during the period 1900–2000 UTC on 12 February was attributed to the mesoscale ERA b. At 2130 UTC on 12 February, cumulus clouds weakened and dissipated in the western part of the comma head owing to the sweeping southward movement of the cold air (Figure 4f). At 0200 UTC on 13 February, the comma cloud moved northeastward, and the surface temperature over north Shandong dropped to below 0 °C (Figure 4h). Two mesoscale snowfall areas (d and e) were formed in the western portion of the comma head and were weaker than the mesoscale ERAs (Figure 4h). The mesoscale snowfall areas produced snowfall of 3.3 mm in Dongying and 3.9 mm in Penglai during 0100–02000 UTC on 13 February.

To compare the difference between rainfall and snowfall areas, we selected two cross sections of radar reflectivity through rainfall and snowfall areas to analyze. A cross section of ERA at 1800 UTC on 12 February (Figure 5a) shows that the rainfall echoes were composed of multiple isolated and upright convective cells, with the core of these convective cells between 2 and 3 km and the 0 °C isotherms at the height of about 2 km (not shown). These high values of radar reflectivity occurred around the freezing level, indicating they are a bright band. Convective cloud echoes of reflectivity > 35 dBZ reached nearly 4 km and the cloud top of some convective cells extended up to 8–9 km, in which the strongest reflectivity was greater than 45 dBZ. However, compared with rainfall echoes, different reflectivity features were found in the snowfall echoes. A cross section through snowfall area at 0200 UTC on 13 February (Figure 5b) shows that snow echoes were also composed of multiple isolated cells and most cells were wider than rainfall cells, in which the intense reflectivity cores were less than 35 dBZ, extending from the surface to no higher than 3 km. The bright band was not found in the snowfall area. The cells near 37.2° N and 37.8° N developed intensively and in their mature stage, with reflectivity > 20 dBZ reaching about 4 km, corresponding to the observed heavy snow. The cells at 36.8° N were in their initial stage, with reflectivity > 20 dBZ below 2 km.

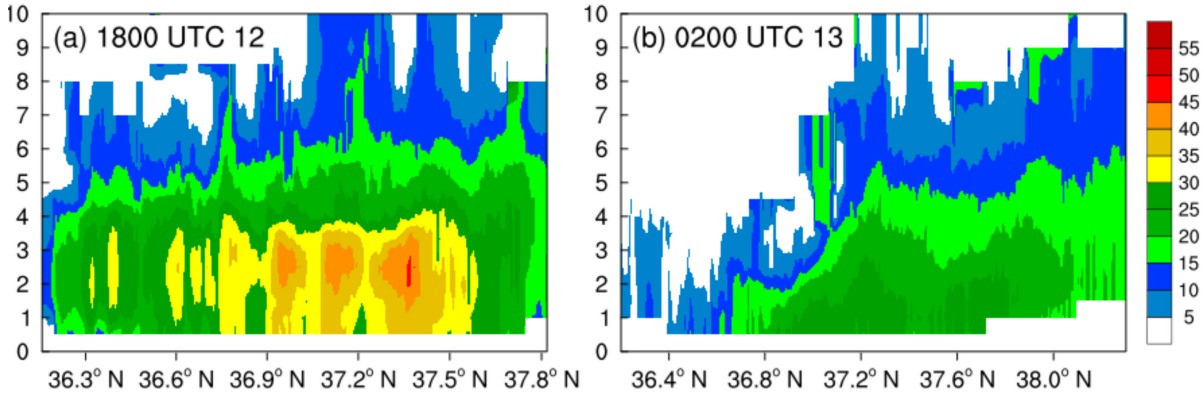

Figure 5. Vertical cross section of radar reflectivity (unit: dBZ) from the mosaic radar reflectivity data along (**a**) intense ERA (see Figure 4d) and (**b**) snowfall areas (see Figure 4h) at (**a**) 1800 UTC on 12 February and (**b**) 0200 UTC on 13 February 2016, respectively.

In summary, multiple echo strips consolidated to form the comma cloud pattern. The comma head corresponded to the warm front clouds, which were dominated by stratiform clouds with scattered cumulus clouds. The tail of the comma cloud corresponded to the cold front clouds, which were dominated by convective clouds in the early stage of formation. After the formation of the Jianghuai cyclone, the echoes rotated cyclonically, and the convective elements in the comma head grew in coverage and extended in a northeast–southwest orientation, contributing to an intense rainfall rate. The cumulus clouds were significantly weakened as the tail of the comma cloud moved to the sea. Associated with the sweeping movement of the cold air, the cumulus clouds in the western portion of the comma head weakened and formed mesoscale snowfall areas, which is also different from the well-defined single-banded structure within the comma head of extratropical cyclones in the northeastern United States in terms of intensity and organization [18].

The height of rainfall echoes was higher and stronger than snowfall echoes, with the obvious bright band at 2–3 km and that of snowfall with no bright band. This is mainly because ice crystals and snowflakes have much smaller scattering than water droplets and less attenuation of microwave radiation.

4. Verification of Model Results

First, we evaluated the performance of the simulation by comparing 24 h of accumulated precipitation from the rain gauge (Figure 6a) with the WRF simulation in the 4 km run (Figure 6b). It is shown that the location, intensity, and coverage of the precipitation were reproduced reasonably well by the model, except that the precipitation in the western Shandong peninsula was larger than observed. The northeast–southwest-oriented precipitation band and maximum precipitation in central Shandong Province were close to the observed, with the simulated maximum precipitation of 55.0 mm quite close to the observed amount of 55.9 mm.

To further demonstrate the model's capability of reproducing the precipitation in detail, we focus on the intense precipitation area in central Shandong Province, as highlighted by the rectangular box in Figure 6a, where most rain gauge stations received more than 30 mm of precipitation. Figure 6c compares the time series of the box-averaged hourly precipitation rates between the observation and the simulation. The model reproduced a similar evolution of the intense precipitation over central Shandong Province. The observed hourly precipitation experienced two stages: (i) a growth stage from 1200 to 2000 UTC on 12 February, during which the hourly precipitation rate increased continuously, except for maintaining high values between 1800 and 2000 UTC on 12 February, and (ii) a weakening stage, in which the precipitation rate decreased after 2000 UTC on 12 February (Figure 6c). The simulated precipitation peak occurred at 1600 UTC on 12 February, which was 2 h earlier than the first observed higher value or 4 h prior to the observed peak value. The

model appears to fail in reproducing the continuous intense precipitation rate between 1800 and 2000 UTC on 12 February and the slowly decreasing precipitation rate after 2300 UTC on 12 February. The simulated precipitation increased a little after 2300 UTC, with a rate of about 1 mmh^{-1} larger than observed (Figure 6c). These simulated errors appear to be responsible for the use of large-scale initial conditions without any mesoscale details, spin-up of the model, and uncertainties associated with the model physical scheme.

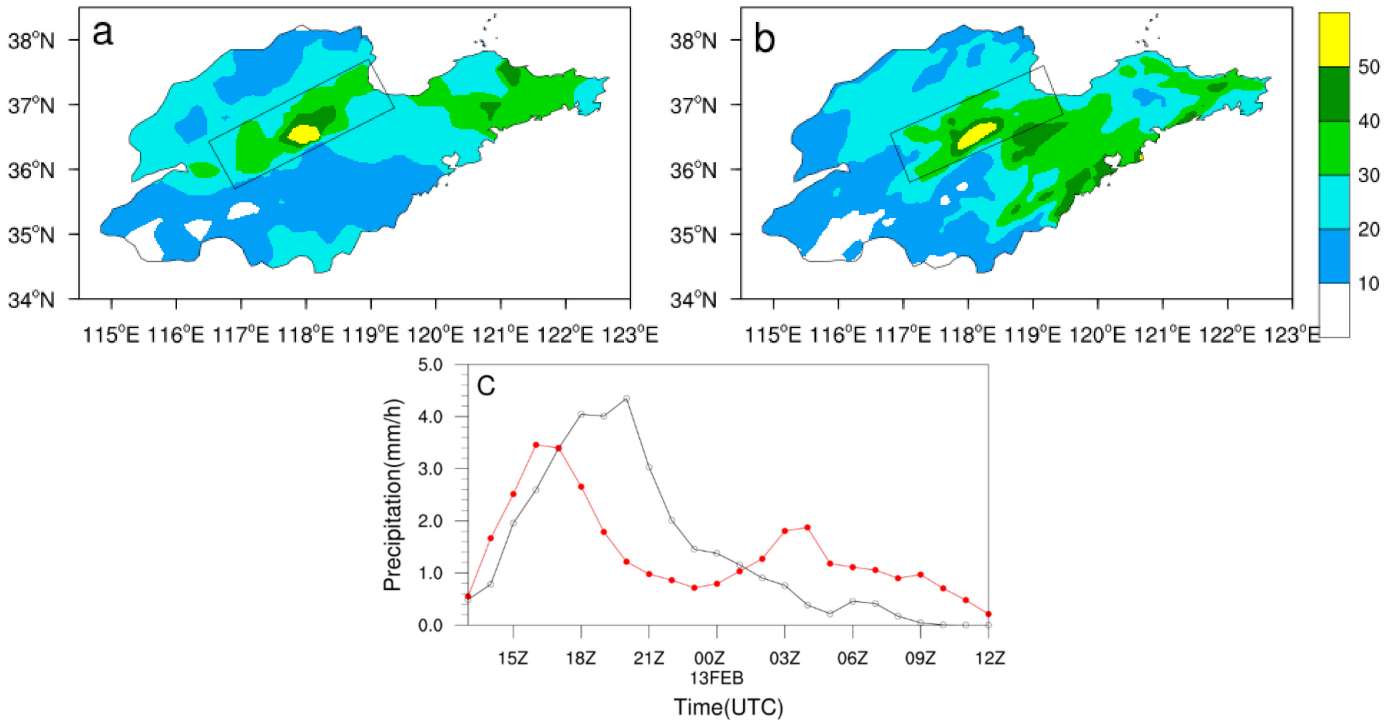

Figure 6. Distribution of the 24 h accumulated precipitation (unit: mm) during the period 1200 UTC on 12 to 1200 UTC on 13 February 2016 derived from (**a**) rain gauge observations and (**b**) the model simulation from the 4 km domain. The black rectangular box denotes the control region. (**c**) Time series of the hourly precipitation (unit: mm·h^{-1}), averaged over the rectangular box during the period from 1200UTC on 12 to 1200 UTC on 13 February 2016 between the observations (black line) and the 4 km domain simulation (red line).

Second, we examined the observed and simulated environmental conditions. The comparison of the analyzed (Figure 7a) and the simulated geopotential height, temperature, and wind fields at 850 hPa by 1800 UTC (Figure 7b) clearly shows that the vortex was well captured with a shear line cross central Shandong. The simulated low-level jet was close to the observation, with the jet core a little stronger and the jet not extending to the northern Jiangsu as observed. Additionally, the simulated temperature was similar to the observation. Compared with the observation, the simulated surface cyclone was generated at 1800 UTC on 12 February, with similar intensity and shift a little to the south (Figure 7c,d). The simulated cyclone moved at a similar speed and direction in the first 12 h and moved northward after 0600 UTC 13 (Figure 7c), with a very small eastward component, which may be one of the reasons for the deviation in precipitation between the simulated and the observed. Other weather systems, such as the 500 hPa westerly trough and 200 hPa subtropical high jet, were all reasonably well reproduced by the model (not shown).

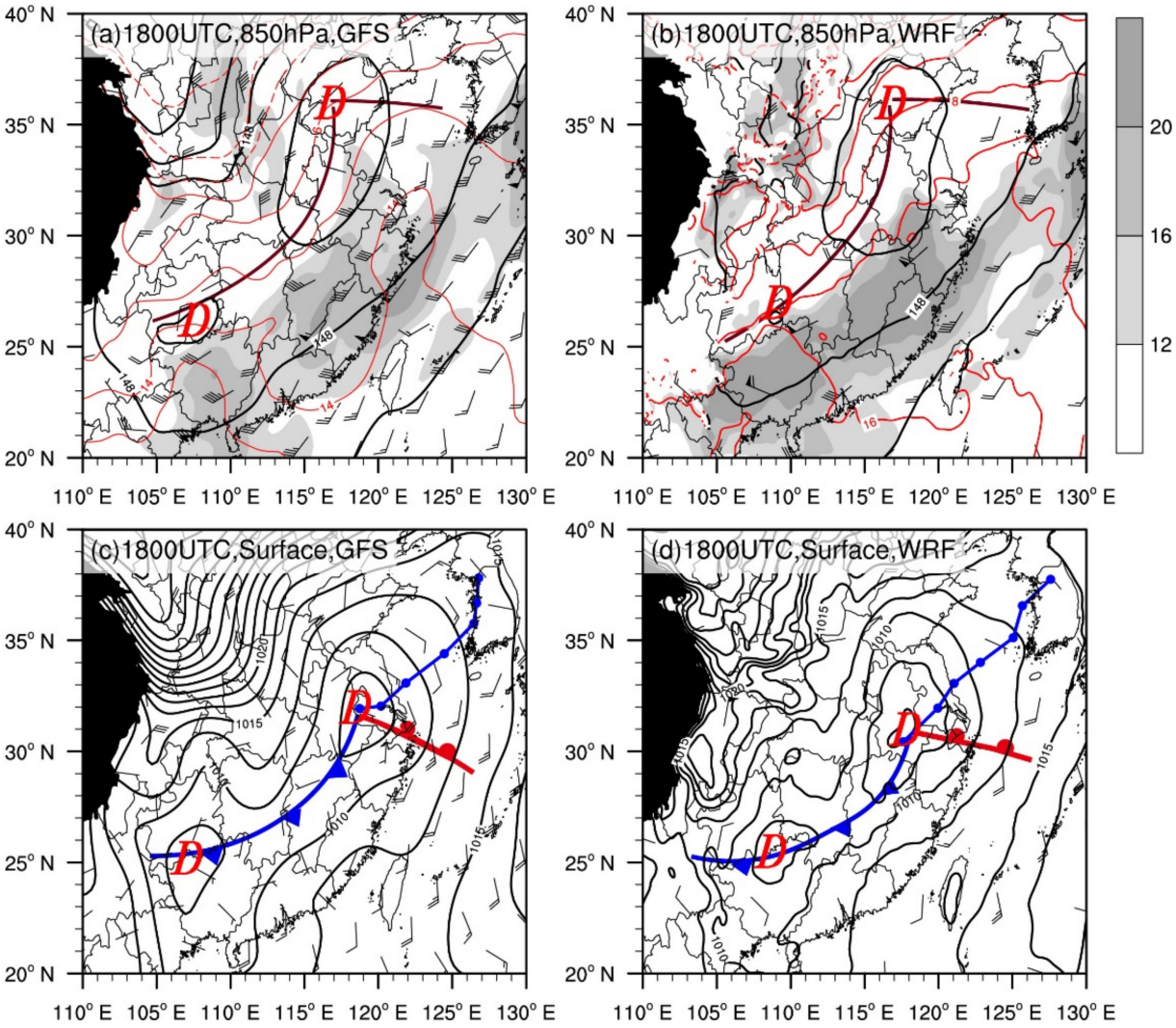

Figure 7. Comparison of (**a**,**b**) geopotential height (black solid lines; unit: dagpm), temperature (red lines; unit: °C), wind speeds $\geq$ 12 m·s^{-1} (shaded), wind barbs at 850 hPa, (**c**,**d**) sea level pressure fields (black lines; unit: hPa), surface low-pressure centers (D), and fronts from analysis (**a**,**c**) and the 12 km-grid simulation (**b**,**d**). The brown thick lines in (**a**,**b**) denote shear lines. The blue lines and blue dots in (**c**,**d**) denote the track of the cyclone from 1800 UTC on 12 to 0600 UTC on 13 Feb at 3 h intervals from NCEP GFS data and WRF model, respectively.

Figure 8c,d show the skew T–logp diagrams at the Zhangqiu sounding station (shown in Figure 2a) from the 4 km run at 1200 UTC on 12 February and 0000 UTC on 13 February 2016, respectively. Compared with Figure 8a,b, the simulated temperature profile and dew-point temperature profile with height exhibit similar patterns and changes except for the difference in dew-point temperature above 200 hPa between the simulation and observation. It was relatively humid below 500 hPa but relatively dry at higher levels with obvious inversion below 800 hPa at 1200 UTC on 12 February. The air below 300 hPa became very moist and nearly saturated at 0000 UTC on 13 February, with an inversion between 700 and 800 hPa. Similar to the observation, the simulated low-level winds were veering with height, and wind changes from southeasterly winds to northeasterly winds at low-level (below 850 hPa) from 1212 UTC on 12 to 0000 UTC on 13 February. Both observation and simulation show a shallow cold layer near the surface at 0000 UTC 13 (Figure 8).

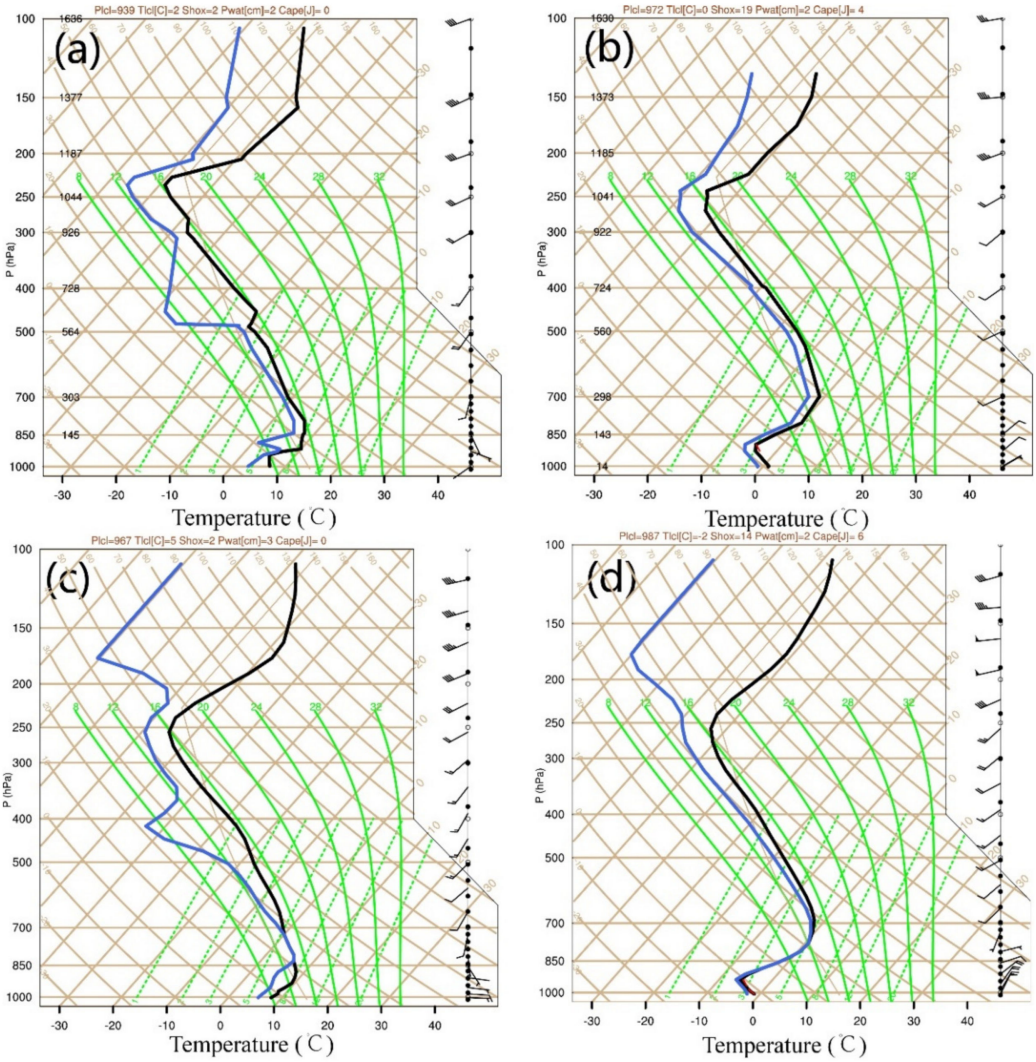

Figure 8. Skew T-logp diagrams at Zhangqiu sounding station from (**a**,**b**) observation and (**c**,**d**) the WRF run at (**a**,**c**) 1200 UTC on 12 February and (**b**,**d**) 0000 UTC on 13 February.

Third, we compared the radar reflectivity between the simulated results from 4 km domain and the mosaic radar reflectivity data. The model produced echo strips over northwestern and central Shandong at 1200 UTC on 12 February (Figure 9a,b) with width, length, and intensity close to the observed, but the echo strips over southeastern Shandong were a little weaker than observed. Moreover, the model reproduced the merger of these echo strips to form the comma head (Figure 9d,f,h–j) and mesoscale ERAs of radar reflectivity > 35 dBZ in central Shandong, which were similar to their observed counterparts in position and intensity. However, the simulated ERAs shifted a little to the north, about one hour earlier than observed. In addition, the model failed to reproduce the cold front clouds; it produced a much smaller area of echoes over southeastern Shandong and northern Jiangsu (Figure 9i,j). These differences in timing and coverage could be attributed to the precipitation spin-up and uncertainties in association with the model physical scheme. The simulated errors over southeast of Shandong might be responsible for the simulated low-level jet errors, which did not extend northward as observed (Figure 7d). At 0100 TUC on 13 February, the model reproduced the movement of the comma head and weakened reflectivity in the western portion of the comma head (Figure 9k,l).

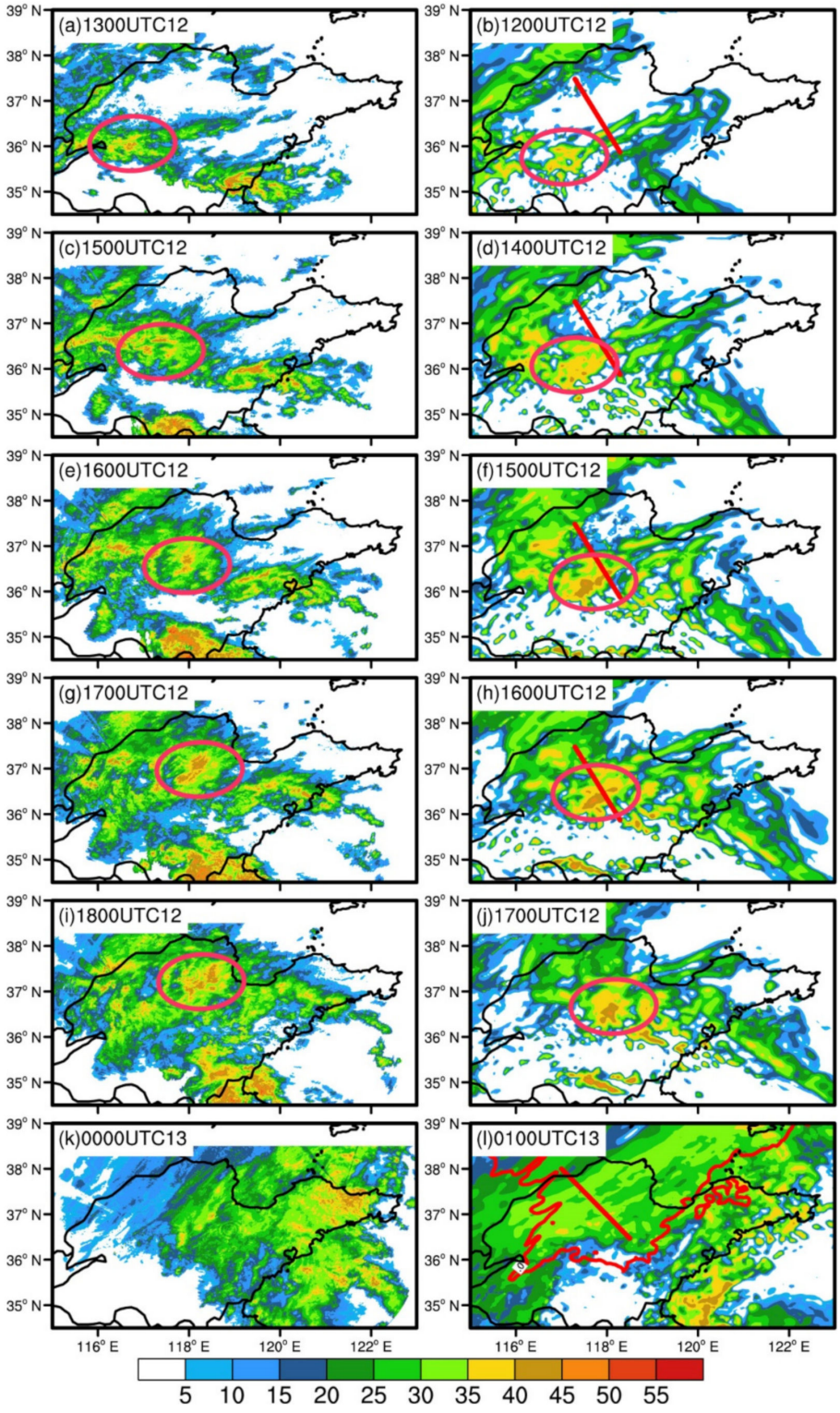

Figure 9. Comparison of radar reflectivity (unit: dBZ) between (**a**,**c**,**e**,**g**,**i**,**k**) observations and (**b**,**d**,**f**,**h**,**j**,**l**) the 4 km domain simulation at (**a**) 1300 UTC 12, (**b**) 1200 UTC 12, (**c**,**f**) 1500 UTC 12, (**d**) 1400 UTC 12, (**e**) 1600 UTC 12, (**f**) 1500 UTC 12, (**g**) 1700 UTC 12, (**h**) 1600 UTC 12, (**i**) 1800 UTC 12, (**j**) 1700 UTC 12, (**k**) 0000 UTC 13, and (**l**) 0100 UTC 13 February 2016, the red lines in (**b**,**d**,**f**,**h**,**l**) represent the location of the cross section used in Figures 10a, 11a, 12a, 13a, and 14a. The red contour in (**l**) represent 0 °C isotherms at the surface. The red ellipses indicate the location of the mesoscale rainfall areas of interest.

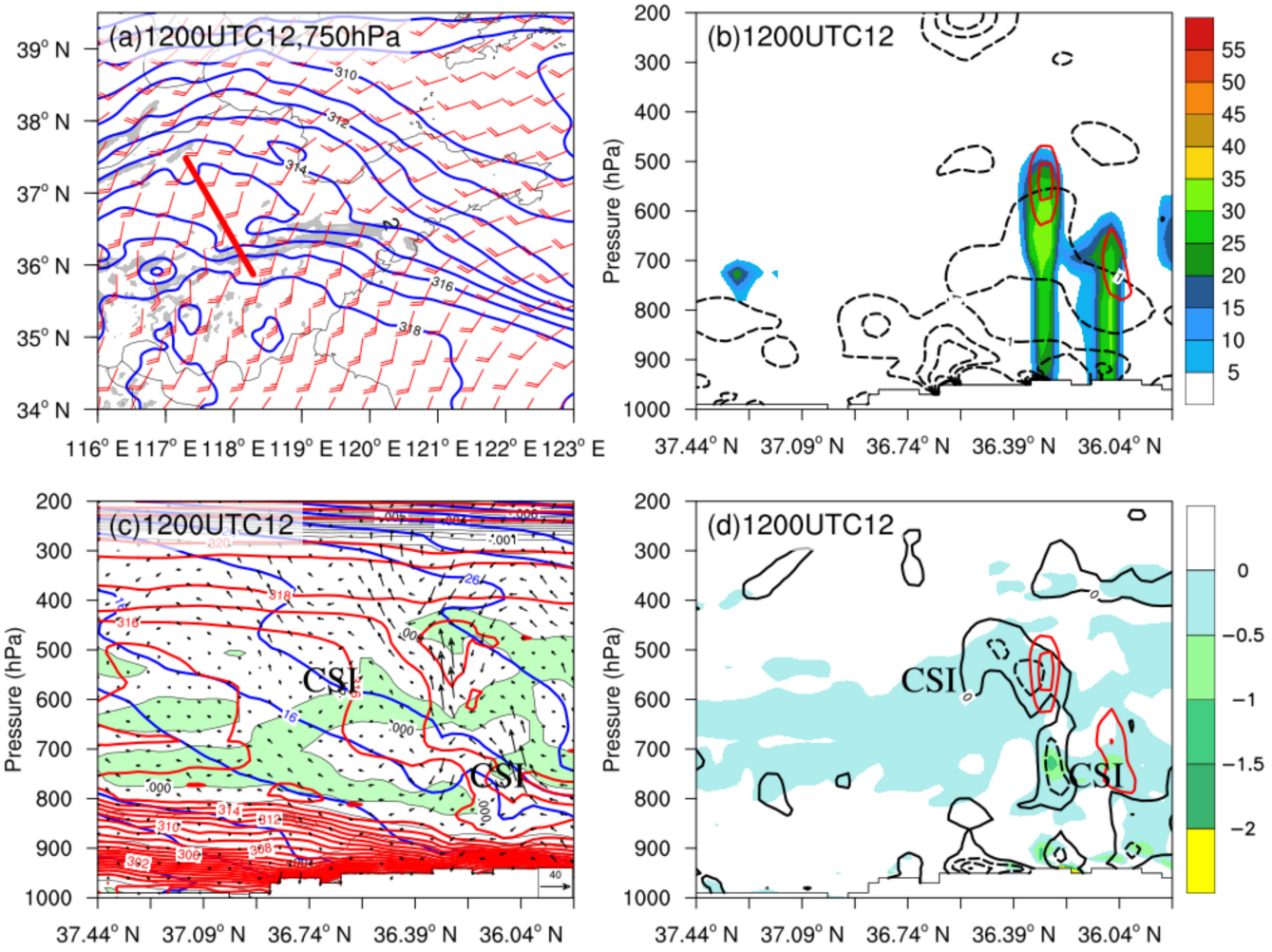

Figure 10. (**a**) The 4 km-grid simulated 750 hPa frontogenesis function (shaded; unit: K (100 km·h)$^{-1}$), saturation equivalent potential temperature (blue lines; contoured every 1 K), and wind barbs (unit: m·s^{-1}) valid at 1200 UTC on 12 February 2016. (**b**) Cross section of the 4 km grid simulated radar reflectivity (shaded; unit: dBZ), frontogenesis function (black dashed lines; unit: K · (100 km·h)$^{-1}$), and ascent (red lines; contoured every 0.2 m · s^{-1}, and starting from 0.2 m · s^{-1}) valid at 1200 UTC on 12 February 2016. (**c**) Cross section as in (**b**) but with saturation equivalent potential temperature (red lines; unit: K), M (blue lines; unit: m·s^{-1}), area of ($\frac{\partial \theta_{es}}{\partial p} > 0$) (green shaded), and vertical circulation. (**d**) Cross section as in (**b**) but with EPV (shaded where negative according to scale), negative absolute vorticity (black dashed lines; contoured every 20 × 10^{-5} s^{-1} s^{-1},) and microphysical heating rate (red lines, contoured every 8 K·s^{-1}, and starting from 8 K·s^{-1}). CSI in (**c**,**d**) denote regions of CSI.

In summary, the model reasonably captured the intensity, evolution, and duration of the precipitation in central Shandong Province, except that the peak precipitation time was earlier than observed, and the peak did not last as long. Moreover, the WRF simulation well reproduced the atmospheric conditions and the evolution of the main weather systems. The occurrence and development of the mesoscale precipitation areas over central Shandong were also reproduced, with the position shifting a little to the north and about one hour earlier than observed.

The focus of this study is on the evolution of the intense precipitation over central Shandong Province, so the shortcomings of the simulation do not affect our analysis. We are confident that the numerical simulation results can be used for further study.

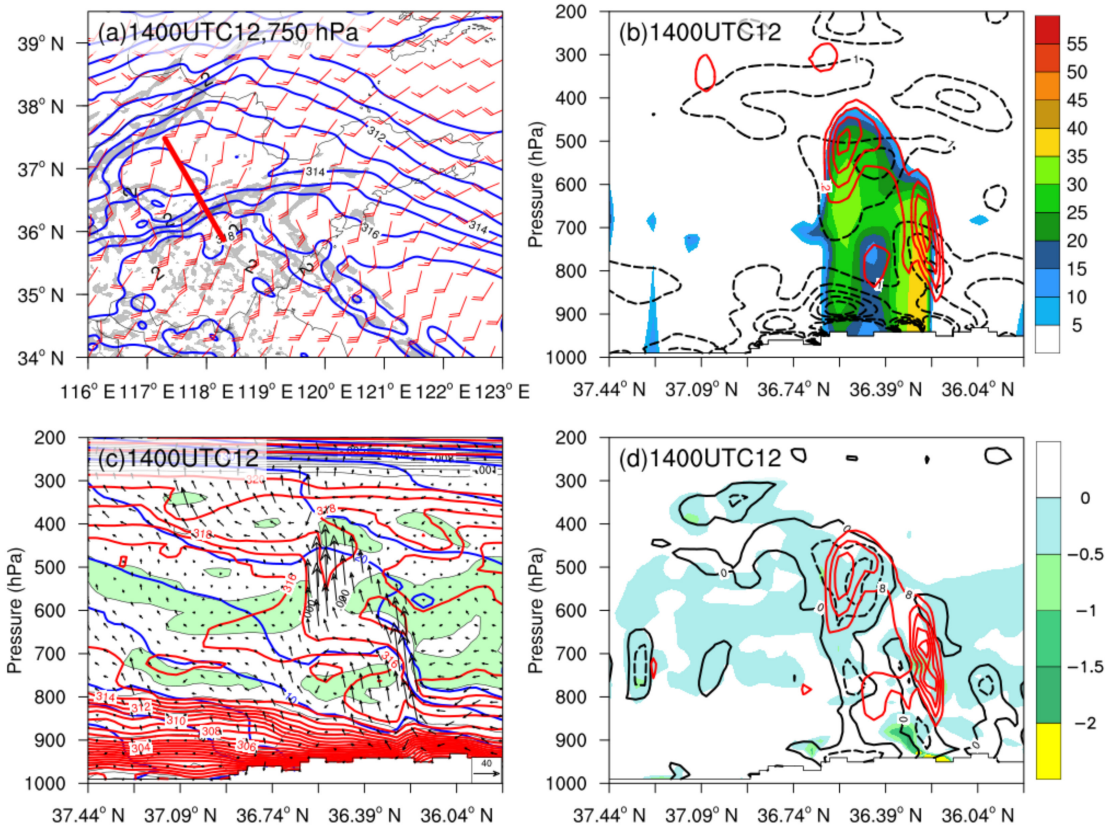

Figure 11. As in Figure 10, but for the 4 km run valid at 1400 UTC 12 February 2016.

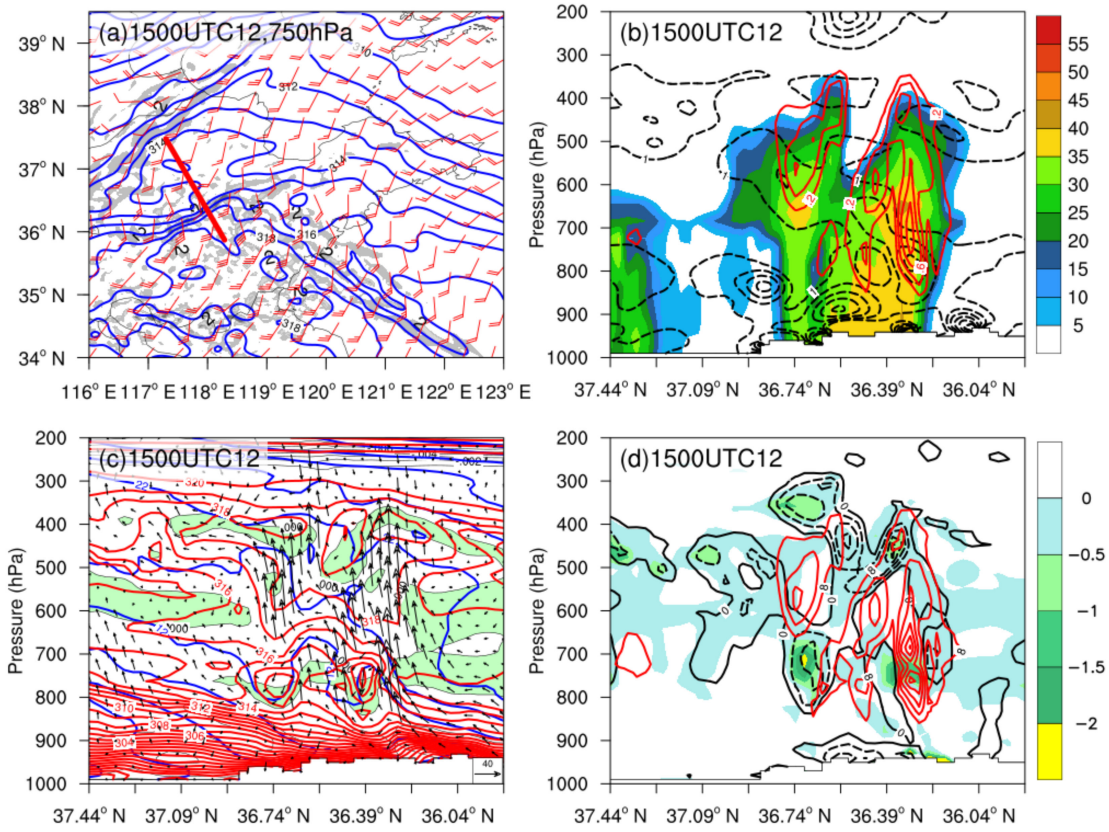

Figure 12. As in Figure 10, but for the 4 km run valid at 1500 UTC 12 February 2016.

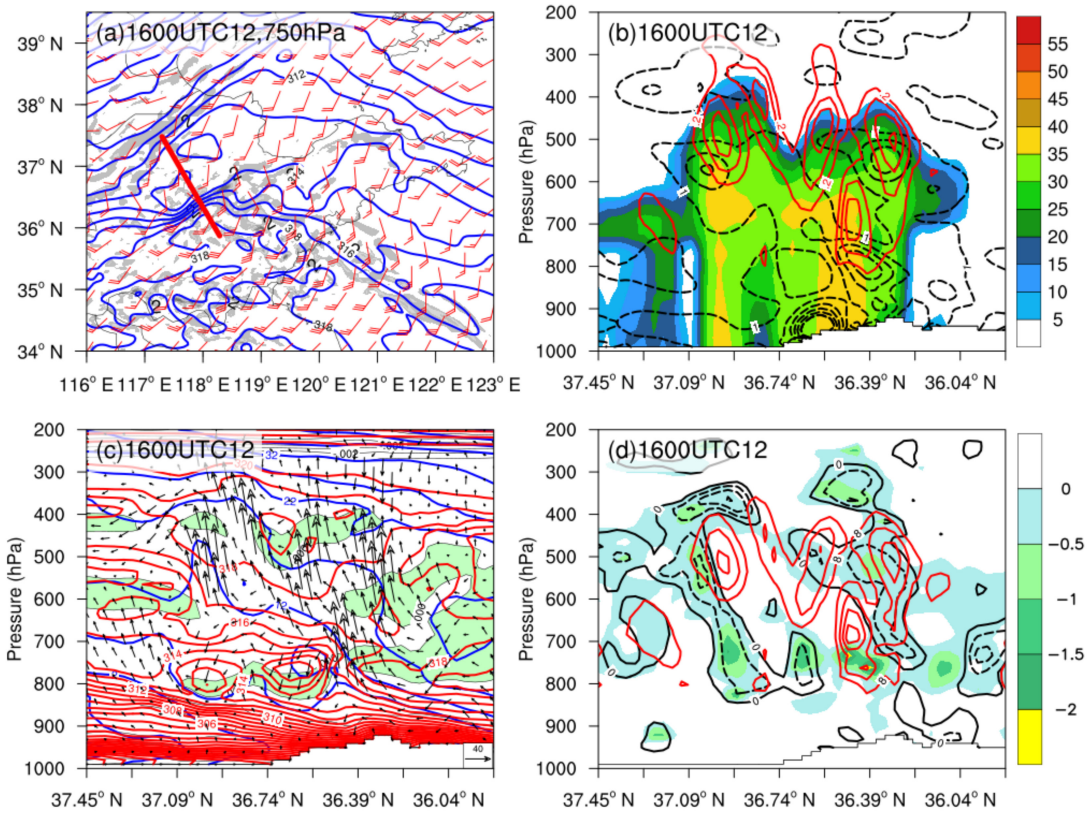

Figure 13. As in Figure 10, but for the 4 km run valid at 1600 UTC 12 February 2016.

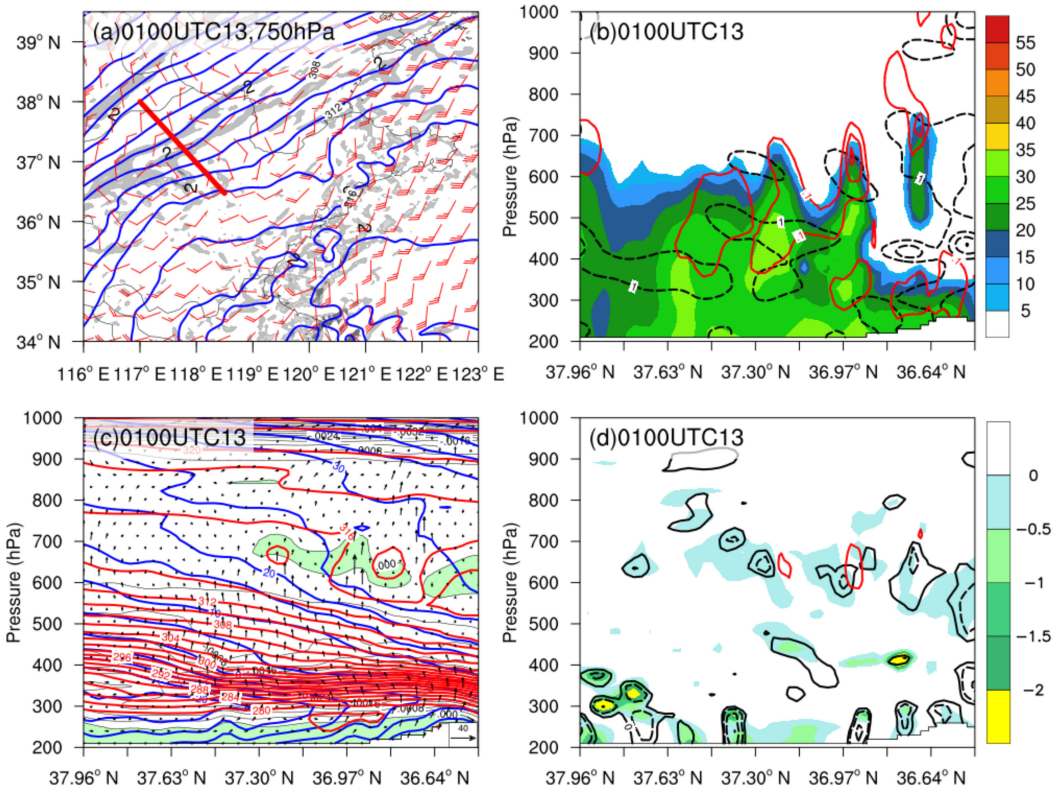

Figure 14. As in Figure 10, but for the 4 km run valid at 0100 UTC 13 February 2016, the contours are the same as Figure 10 except for saturation equivalent potential temperature in (**a**) contoured every 2 K, ascent in (**b**) contoured every 0.1 m·s^{-1} and starting from 0.1 m·s^{-1}.

5. Stability and Forcing Mechanisms of Mesoscale Precipitation Areas

From the above analysis, multiple mesoscale rainfall and snowfall areas were observed within the comma head of the cyclone. Then, what were the stability and forcing mechanisms responsible for the formation and development of these mesoscale precipitation areas? In this section, a detailed analysis is performed using the WRF model results. The precipitation was subjectively divided into rainfall stage and snowfall stage.

5.1. Rainfall Stage

The model successfully reproduced the evolution of the main mesoscale ERAs over central Shandong (Figure 9). The life cycle of the ERA is subjectively divided into the initial stage and the development stage.

At 1200UTC on 12 February, the rainfall was in its initial stage. A nearly northeast-southwest-oriented echo strip was located in a region of speed convergence over central and southwestern Shandong, in which a stronger echo cluster with reflectivity > 35 dBZ was located in southwestern Shandong (red ellipse in Figure 9b). The echo cluster was organized poorly, with some echo-free area and weak echo, and connected with two weak and narrow banded reflectivity to the east (Figure 9b). It was enhanced further and organized 2 h later as it propagated northeastward, with sporadic reflectivity > 40 dBZ and was differentiated short bands of reflectivity > 35 dBZ along the cross section (Figure 9d). By 1500 UTC on 12 February, the southern reflectivity band intensified significantly, and the regions of reflectivity > 40 dBZ stretched along a northeast–southwest axis into central Shandong to form an intense ERA (Figure 9f). The ERA developed to its strongest stage during the period 1600–1700 UTC, with the maximum radar reflectivity > 50 dBZ (Figure 9h). The ERA weakened and moved eastward quickly after 1700 UTC on 12 February.

5.1.1. Initial Stage of the ERA

To analyze the stability and the forcing mechanism of the mesoscale rainfall area in the different stages, a fixed cross section perpendicular to the mesoscale ERA (denoted by red lines in Figures 9–14) was analyzed on the 4 km domain.

At 1200 UTC on 12 February, a northeast–southwest-oriented maximum frontogenesis with values exceeding 7 K · (100 km·h)$^{-1}$ was located over central Shandong at 750 hPa, with a larger speed convergence and temperature gradient (Figure 10a), which corresponded to the reflectivity bands. A cross section of reflectivity, frontogenesis, and ascent exhibited two distinct reflectivity bands between 36.39° N and 36.04° N, with the height of the 30 dBZ contour extending to nearly 550 and 650 hPa, respectively (Figure 10b). The two reflectivity bands were associated with two regions of ascent: the northern one maximized at over 0.4 m s^{-1} at 550 hPa, while the southern one maximized at over 0.2 m s^{-1} at about 700 hPa (Figure 10b). Two regions of ascent were forced by sloping frontogenesis maxima, with the ascent maximum on the warm side of the frontogenesis maxima (Figure 10b). The microphysical latent heat was consistent with the ascent, and two regions of latent heat heating rates > 8×10^{-4} K · s^{-1} were uniformly distributed in the two regions of ascent (Figure 10d).

A cross section of stability shows that numerous regions of negative EPV existed in the 850–300 hPa layer (Figure 10d), with the θes field and distribution of ($\frac{\partial \theta_{es}}{\partial p} > 0$), indicating that most of these negative EPV regions were associated with CI (Figure 10c). Two negative absolute vorticities appeared below 800 hPa above the front in the EPV field, with two regions of negative absolute vorticity in the 850–600 hPa and 620–450 hPa layer on the poleward periphery of the two sloping ascent maxima (Figure 10d), indicative of II. A small portion of the negative EPV region between 36.21° N and 36.04° N in the 800–700 hPa layer exhibited conditional stability and inertial stability, and the θe surfaces are more steeply sloped than the M surfaces (Figure 10c), with relative humidity larger than 90% (not shown), indicative of CSI. Moreover, some regions in the 600–500 hPa layer to the north of the reflectivity band were marked by CSI. These instabilities lay above the maximum frontogenesis, and the ascending motion forced by frontogenesis

extended above the position of maximum frontogenesis [53–55]. Thus, the modeled rainfall associated with the two short bands was likely a result of the release of elevated CI, CSI, and II by frontogenetical forcing. It was noted that CSI was between the two bands and to the north of the band, which is favorable for the merger and expansion of the band.

5.1.2. Development of the ERA

By 1400 UTC on 12 February, the large temperature gradient had been created by the development of a local temperature minimum along a southwest–northeast axis to the north of these reflectivity bands (Figure 11a). The combined effect of this large temperature gradient with the strong speed convergence resulted in frontogenesis values exceeding 18 K · (100 km · h)$^{-1}$ at 750 hPa (Figure 11a). Because the two short bands had consolidated into a whole (Figure 9d), a corresponding cross section shows that the reflectivity core of the northern band was between 550 and 750 hPa, and the southern band up to 700 hPa from the surface (Figure 11b). These reflectivity cores were associated with separate ascent maxima; the northern one neared 0.8 m s^{-1} at about 500 hPa (Figure 11b). The frontogenesis associated with the southern band increased and centered at 700 hPa, with an ascent exceeding 0.9 m s^{-1} above this level (Figure 11b).

The corresponding stability fields indicate enhanced II and a small area of CI associated with the two bands (Figure 11c,d). For the northern band, however, CI was absent, and II was enhanced at this time. The M surfaces near the sloping ascent region between 36.74° N and 36.39° N were buckled (Figure 11c), indicating Delta-M adjustment had occurred. Thus, an enhanced negative absolute vorticity region was found on the poleward periphery of the sloping ascent maxima associated with upper-level II. The microphysical latent heat associated with the precipitation increased significantly. Two strong heating centers corresponded to the two reflectivity cores near 500 hPa and 700 hPa, respectively, with the maximum heating rate exceeding 40 × 10^{-4} K·s^{-1} (Figure 11d), which corresponded well to the downward concave of the θ_e contours within the sloping ascent area.

The existence of II in the frontal zone has been documented in previous studies [41,56–60]. Delta-M adjustment is the generation of localized negative PV regions by advection associated with convective storms [41]. The Delta-M adjustment is generated when the air parcels are lifted from the lower level, which has smaller momentum than the upper-level environmental air owing to momentum conservation in the baroclinic atmosphere. The air parcels would obtain inertial acceleration to move northward along the isentropic surface, resulting in slantwise convection [42]. CI, which represents the potential for upright convection, was present in the initial stage of precipitation (e.g., Figure 10c) in this case. However, CI was absent, and II was enhanced with buckling of the M surfaces near the surface between 36.57° N and 36.39° N at 1300 UTC on 12 February (not shown) and enhanced condensational heating. The II was consistent with the condensational heating by the precipitation itself and to the north of the condensational heating (Figure 11d). Associated with the release of the condensational heating, the air parcels in low levels with low M rose vertically to a higher level to generate an M anomaly. Thus, the slantwise ascent between 36.74° N and 36.39° N was enhanced owing to Delta-M adjustment (Figure 11c). Given the presence of the II in the absence of upright convection, it seems likely that the presence of II at this time is a diabatic signature of the band itself, which is similar to the process discussed by Novak et al. [45].

By 1500 UTC on 12 February, the winds at 750 hPa exhibited a sharp cyclonic wind shift near the ERAs, with strong southwest winds on the south side of the ERAs and southeast winds on the north side of the ERAs (Figure 12a). A corresponding cross section shows that these ERAs consolidated and grew in coverage, with the two ERAs extending to above 400 hPa and the northern band's reflectivity core sloping southward from the surface (Figure 12b). The northern ERA exhibited II and delta-M adjustment, and the upper-level outflow evidently enhanced, which was likely responsible for the II. Schultz and Knox [59] suggested that the release of II may cause convection to organize into narrow bands. Blanchard et al. [61] proposed that upper-level II may increase the intensity of

convective systems by enhancing outflow aloft. Thus, the II intensified and organized the ERAs. The southern ERA exhibited enhanced CI, CSI, and II.

Apart from the upper-level slantwise ascent associated with II, the M contours between 36.74° N and 36.04° N were buckled, with a strong slantwise ascent (Figure 12c). Associated with the buckling of the M surfaces, the slope of the θ_e contours to the south of the M contours became steeper, which further enhanced the CSI, with the increasing negative EPV at the surface near 36.39° N between 800 and 600 hPa (Figure 12c,d). The intensification of CSI probably result from the release of the condensational heating of precipitation. The latent heat made the slope of the θ_e surfaces increase, which was beneficial to the generation of CSI and even CI.

5.1.3. Mature Stage of the ERA

The mature stage of the southern ERA occurred at 1600 UTC on 12 February, when the ERA was near peak intensity. The temperature gradient had intensified within the region of maximum speed convergence (Figure 13a). The coincidence of this large temperature gradient with the intense speed convergence resulted in the maximum frontogenesis value exceeding 26 K · (100 km·h)$^{-1}$ (Figure 13a), which was the strongest frontogenesis over central Shandong. The corresponding cross section shows that the reflectivity cores were nearly upright (Figure 13b). The CSI in the 850–600 hPa layer near the surface at about 36.39° N enhanced further, with the maximum negative EPV increasing to −2 PVU (Figure 11d), and the coverage of the ascent increased. Associated with the release of CSI, the coverage of the REA enlarged (Figure 9h), corresponding to the modeled peak hourly precipitation rate (Figure 6c). The hourly precipitation rate in the vicinity of 36.57° N was more than 8 mm·h^{-1}. Compared with the previous time, large-amplitude buckling of the M surfaces was produced at the position of the release of CSI. The maximum frontogenesis of more than 26 K (100 km·h)$^{-1}$ was between 850 and 750 hPa (Figure 13b), and the CSI was also the strongest, indicating that the secondary circulation likely promoted the development of CSI.

The ascending branch of the secondary circulation caused by frontal forcing promoted the upward transport of warm and moist air and initiated convection. When precipitation develops, the release of the condensational latent heating of precipitation leads to a reduction in EPV, which promotes the development of CSI. At the same time, latent heat heating will further enhance the frontogenetical forcing, promote the development of frontal secondary circulation, and then enhance precipitation.

5.2. Snowfall Stage

Accompanying the formation of the cyclone, the cold air swept southward. The simulated surface temperature decreased below 0 °C; thus, snow occurred. The winds at 750 hPa at 0100 UTC on 13 February changed into northwest winds over northwestern Shandong, with strong frontogenesis in the snowfall area (Figure 14a). The corresponding cross section through the snowfall area (Figure 14a) shows that the snowfall reflectivity was composed of stratiform clouds, with the cloud top at about 700 hPa, and three cells can be differentiated. Three cells were associated with three regions of ascent, the strongest of which was over 0.3 m·s^{-1} near the surface at 36.97° N (Figure 14b). These regions of ascent were also forced by sloping frontogenesis maxima. However, the frontogenesis maxima and ascent are smaller than those in rainfall areas, and the corresponding latent heating was weak. The corresponding stability shows elevated CI in the layer of 600–700 hPa and small coverage II and CSI in the snowfall area (Figure 14c,d).

In summary, the rainfall and snowfall occurred in an environment of II, weak elevated CI, and CSI. In the rainfall stage, the II in the middle and upper levels made the air parcels obtain inertial acceleration moving northward, increasing the upper-level outflow, which was conducive to the strengthening and organization of the precipitation system. The weak CI in the lower level was close to the neutral stratification, and there was CSI. The frontal forcing provided the dynamic conditions for the release of unstable energy.

The condensational heating played an important role in the enhancement of the multiple instabilities, and the latent heat release would have further enhanced the frontogenetical forcing. In the snowfall stage, the instabilities were weaker and shallower than those in the rainfall stage, resulting in a weak ascent.

6. Summary and Discussion

A record-breaking rain–snow event produced by multiple mesoscale elongated precipitation areas within the comma head of a Jianghuai cyclone in Shandong Province, China, on 12–13 February 2016 was investigated using FY-2G satellite data, Doppler radar observations, and a WRF model simulation at 4 km grid spacing. In this paper, we have examined the mesoscale evolution of precipitation clouds and the stability and forcing mechanisms responsible for the formation, organization, and maintenance of the elongated precipitation areas. The main conclusions can be summarized as follows.

The merger of a 500 hPa middle branch trough and a southern branch trough and moving to the west of Shandong Province was responsible for the cyclogenesis and precipitation. The strong low-level southerly jets provided abundant water vapor and energy for precipitation, whereas the low-level vortex and associated shear line were conducive to low-level convergence and ascent. After the formation of the cyclone, the cold air moved southward rapidly, and the transition from rain to snow occurred.

The comma-head cloud of the Jianghuai cyclone developed from four echo strips. In the initial stage of the cyclone, the warm front clouds were dominated by stratiform clouds with scattered convective clouds, while the cold front clouds were mainly composed of convective clouds and weakened after moving over the sea. Accompanying the formation of the cyclone, the radar echo had a cyclonic rotation and elongation, forming a number of mesoscale EPAs of reflectivity > 30 dBZ. Intense rain and snow were associated with the EPAs in the stratiform clouds.

The formation and development of the EPAs coincided with the activities of a low-level shear line and the associated increase in frontogenesis. The precipitation developed in an environment of CI, II, and CSI. In the initial stage of the ERA, rainfall was initiated by the frontogenetical forcing in the presence of elevated CI, and II was generated by upright convection. During the development stage of the ERA, the CI was absent, and condensational heating was enhanced; upper-level II occurred in the absence of upright convection, and the presence of II was a diabatic signature of the precipitation. Upper-level II intensified the precipitation systems by enhancing the upper-level outflow, and II may have caused the EPAs' organization, which is consistent with the findings reported by Blanchard et al. [61] and Schultz and Knox [59].

The frontogenesis provided the dynamic condition for the release of the instability. The ascending branch of the frontal secondary circulation promoted the upward transport of warm and moist air and initiated convection. During the development stage of the ERA, the release of the condensational heating of precipitation resulted in a decrease in EPV and promoted the development of CSI. At the same time, latent heat further enhanced the frontogenetical forcing, promoted the frontal secondary circulation, and thus enhanced precipitation.

The stability and forcing mechanisms of the rain–snow event were similar to other observed cases of banded precipitation in the comma head of extratropical cyclones [18,19] but did not form a well-defined banded structure. This is probably because the Jianghuai cyclone was much weaker and did not occlude, with the weaker and shallower frontogenesis in the snowfall areas. The banded structure usually occurs in the snowfall area within the comma head of an occluded cyclone. Novak et al., found that the banded exhibited stronger and deeper frontogenesis and weaker conditional stability than the nonbanded [18,19]. In our case, the frontogenesis was weaker and not deeper enough in the snowfall area, so no banded structure formed.

By the way, we have found clear snow bands over northeast China through the preliminary statistical study of the snow events associated with extratropical cyclones

in the cold season, but the length (less than 250 km) is not long, and the intensity (less than 30 dBZ) is not intense as those defined by Novak et al. [18]. A new definition of a banded structure needs to be given in China. The reason could be attributed to the different synoptic environments and terrain conditions between China and America. In addition, their snowfall intensity is not comparative; the snow intensity in America is so heavy than that in China, so the bands are different. Our group is conducting a statistical analysis of mesoscale precipitation bands within the comma head of extratropical cyclones, and the general results will be obtained.

Although the model reproduced similar EPAs, the deviation time and intensity existed between the observation and simulation because of model deficiencies. The cold season precipitation mechanism is complex, with multiple instabilities occurring simultaneously. Therefore, it is difficult to study through observations only, and the aid of a model can improve understanding of the structural and dynamic evolution of mesoscale precipitation associated with Jianghuai cyclones. Future work should draw upon sensitivity simulations to reveal the relationship between condensational heating and multiple stabilities, as well as the effect of topography.

Author Contributions: Conceptualization, Y.Z. and X.L.; investigation and methodology, Y.Z. and C.Y.; software, formal analysis, and validation, X.L. and S.L.; resources, C.Y.; writing—original draft preparation, Y.Z.; writing—review and editing, Y.Z.; supervision, Y.Z. All authors have read and agreed to the published version of the manuscript.

Funding: This study was funded by the National Natural Science Foundation of China (41975055) and the National Key Research and Development Program of China (2017YFC1502002).

Institutional Review Board Statement: Not applicable.

Informed Consent Statement: Not applicable.

Data Availability Statement: The dataset of GFS analysis data is available online at https://rda.ucar.edu/datasets/ds084.1/ (accessed on 15 April 2021). The FY-2G satellite data were obtained from the National Satellite Meteorological Center of China Meteorological Administration, which are available at http://satellite.nsmc.org.cn/PortalSite/Data/ (accessed on 15 April 2021). The radar data were obtained from Shandong Meteorological Observatory. The WRF model is freely available at https://www2.mmm.ucar.edu/wrf/users/download/get_source.html (accessed on 20 July 2017).

Acknowledgments: We wish to thank two anonymous reviewers and academic editors for their constructive comments and suggestions, which helped us improve the manuscript. We would also like to thank the Nanjing University of Information Engineering High-Performance Computing Center provides computing services.

Conflicts of Interest: The authors declare no conflict of interest.

References

1. Zhao, Y.; Lan, X.; Yang, C.F. Analysis of the cloud characteristic and the mechanism of an extreme rainfall-snowfall event associated with cyclones over Changjiang-Huaihe River basin. *Plateau Meteorol.* **2018**, *37*, 1325–1340.
2. Yan, L.F.; Yang, C.F. *Book of Disaster Weather Forecasting Technology in Shandong Province*; China Meteorological Press: Beijing, China, 2014; pp. 182–183.
3. Zheng, L.N.; Jin, J. Analysis on formation mechanism of rare 'Thundersnow' phenomenon in Shandong on 28 February 2010. *Plateau Meteor.* **2012**, *31*, 1151–1157.
4. Yan, Q.; Jiang, D.K.; Chen, C.L. Climatic characteristics of regional snowstorm from 1960 to 2009 in Liaoning province. *J. Meteorol. Environ.* **2012**, *28*, 43–48.
5. Fu, L.; Zhao, Y.; Yang, C.F.; Zhao, L. Statistical characteristics of the northward extratropical cyclone snowstorm affecting Northeast China. *Plateau Meteorol.* **2018**, *37*, 1705–1715.
6. Cai, L.N.; Sui, Y.J.; Liu, D.Q.; Wang, S.; Liu, W.; Wang, T.K. Analysis on an unusual snowstorm event caused by explosive cyclone. *Acta Sci. Nat. Univ. Pekin.* **2009**, *45*, 693–700.
7. Gao, S.Y.; Sun, L.Q.; Liu, T.W.; He, B.C. Diagnostic analysis of an extraordinarily severe snowstorm event in Liaoning province. *Meteorol. Sci. Technol.* **2009**, *37*, 175–180.
8. Yang, X.X.; Wu, W.; Wan, M.B.; Sun, C.Z.; Wang, W.Q.; Diao, X.G. A comparative analysis of two snowstorms in Shandong Province. *Meteor. Mon.* **2012**, *38*, 868–876.

9. Sun, X.; Cai, X.N.; Chen, C.L.; Jia, X.X.; Qiao, X.S. Analysis of the 4 March 2007 heavy snowstorm in northeast China. *Meteorol. Mon.* **2011**, *37*, 863–870.
10. Ren, L.; Yang, W.W.; Tang, Y.; Ren, L.; Yang, W.W.; Tang, Y.; Zhang, H.J.; Wu, Y. Diagnostic analysis of a snow-storm caused by explosive cyclone. *J. Meteorol. Environ.* **2015**, *31*, 45–52.
11. Ren, L.; Zhang, G.H.; Zhou, Y.H.; Chen, X.F. Study on dynamic system of explosive cyclone causing a snow storm in Heilongjiang province. *J. Meteorol. Environ.* **2016**, *32*, 28–36.
12. Yi, X.Y.; Li, Z.C.; Chen, T.; Li, Y. Activities of cold-dry air and its impact on heavy rain–snow processes in North China during March 3–5 2007. *J. Nanjing Inst. Meteorol.* **2009**, *32*, 306–313.
13. Sun, Y.H.; Li, Z.C.; Shou, S.W. A mesoscale analysis of the snowstorm event of 3–5 March 2007 in Liaoning province. *Acta Meteorol. Sin.* **2012**, *70*, 936–948.
14. Sun, Y.H.; Li, Z.C.; Shou, S.W. An investigation into the features and effects of the mesoscale gravity waves as in a snowstorm event. *Acta Meteorol. Sin.* **2015**, *73*, 697–710.
15. Zhao, Y.; Zhu, H.Q.; Lan, X.; Yang, C. Structure of the snowstorm cloud associated with northward Jiang-huai cyclone based on Cloud satsatellite data. *Chin. J. Geophys.* **2018**, *61*, 4789–4804. [CrossRef]
16. Zhao, Y.; Lan, X.; Yang, C.F. Radar echo and airmass structure of the comma head within a Jiang-Huai cyclone in winter. *Acta Meteorol. Sin.* **2018**, *76*, 726–741.
17. Zhao, Y.; Fu, L.; Yang, C.F.; Chen, X.F. Case study of a heavy snowstorm associated with an extratropical dyclone featuring a back-bent warm front structure. *Atmosphere* **2020**, *11*, 1272. [CrossRef]
18. Novak, D.R.; Bosart, L.F.; Keyser, D.; Waldstreicher, J.S. An observational study of cold season–banded precipitation in northeast U.S. cyclones. *Weather. Forecast.* **2004**, *19*, 993–1010. [CrossRef]
19. Novak, D.R.; Colle, B.A.; Aiyyer, A.R. Evolution of Mesoscale Precipitation Band Environments within the Comma Head of Northeast U.S. Cyclones. *Mon. Weather Rev.* **2010**, *138*, 2354–2374. [CrossRef]
20. Baxter, M.A.; Schumacher, P.N. Distribution of single-banded snowfall in central U.S. cyclones. *Weather Forecast.* **2017**, *32*, 533–554. [CrossRef]
21. Ganetis, S.A.; Colle, B.A. The thermodynamic and microphysical evolution of an intense snowband during the Northeast U.S. Blizzard of 8–9 February 2013. *Mon. Weather Rev.* **2015**, *143*, 4104–4125. [CrossRef]
22. Ganetis, S.A.; Colle, B.A.; Yuter, S.E.; Hoban, N.P. Environmental conditions associated with observed snowband structures within northeast U.S. winter storms. *Mon. Weather Rev.* **2018**, *146*, 3675–3690. [CrossRef]
23. Lackmann, G.M.; Thompson, G. Hydrometeor lofting and mesoscale snowbands. *Mon. Weather Rev.* **2019**, *147*, 3879–3899. [CrossRef]
24. Chen, G.X.; Wang, W.C.; Chen, C.T.; Hsu, H.H. Extreme snow events along the coast of the northeast United States: Potential changes due to global warming. *J. Clim.* **2021**, *34*, 2337–2353. [CrossRef]
25. Martin, J.E. The structure and evolution of a continental winter cyclone—Part I: Frontal structure and the occlusion process. *Mon. Weather Rev.* **1998**, *126*, 303–328. [CrossRef]
26. Schultz, D.M.; Vaughan, G. Occluded fronts and the occlusion process. A fresh look at conventional wisdom. *Bull. Am. Meteorol. Soc.* **2011**, *92*, 443–466. [CrossRef]
27. Wiesmueller, J.L.; Zubrick, S.M. Evaluation and application of conditional symmetric instability, equivalent potential vorticity, and frontogenetic forcing in an operational forecast environment. *Weather Forecast.* **1998**, *13*, 84–101. [CrossRef]
28. Nicosia, D.J.; Grumm, R.H. Mesoscale band formation in three major northeastern United States snowstorms. *Weather Forecast.* **1999**, *14*, 346–368. [CrossRef]
29. Bennetts, D.A.; Hoskins, B.J. Conditional symmetric instability—A Possible explanation for frontal rain bands. *Q. J. R. Meteorol. Soc.* **1979**, *105*, 945–962. [CrossRef]
30. Emanuel, K.A. Frontal circulations in the presence of small moist symmetric stability. *J. Atmos. Sci.* **1985**, *42*, 1062–1071. [CrossRef]
31. Xu, Q. Frontal circulations in the presence of small viscous moist symmetric stability and weak forcing. *Q. J. R. Meteorol. Soc.* **1989**, *115*, 1325–1353. [CrossRef]
32. Sanders, F.L.; Bosart, F. Mesoseale structure in the MegaloPolitan snowstorm of 11–12 February1983—Part I: Frontogenetical forcing and symmetric instability. *J. Atmos sci.* **1985**, *42*, 1050–1061. [CrossRef]
33. Sanders, F.L. Frontogenesis and symmetric stability in a major New England snowstorm. *Mon. Weather Rev.* **1986**, *114*, 1847–1862. [CrossRef]
34. Moore, J.T.; Blakley, P.D. The role of frontogenetical forcing and conditional symmetric instability in the Midwest snowstorm of 30–31 January 1982. *Mon. Weather Rev.* **1988**, *116*, 2155–2171. [CrossRef]
35. Novak, D.R.; Waldstreicher, J.S.; Keyser, D.; Bosart, L.F. A forecast strategy for anticipating cold season mesoscale band formation within eastern U. S. cyclones. *Weather Forecast.* **2006**, *21*, 3–23. [CrossRef]
36. Weisman, R.A. The Fargo Snowstorm of 6–8 January 1989. *Weather Forecast.* **1996**, *11*, 198–215. [CrossRef]
37. Emanuel, K.A. Forced and free mesoscale motions in the atmosphere. Collection of Lecture Notes on Dynamics of Mesometeorological Disturbances. In Proceedings of the Cooperative Institute for Meteorological Satellite Studies symposium, Norman, OK, USA, 22 April 1980; pp. 191–259.
38. Jascourt, S.D.; Lindstrom, S.S.; Seman, C.J.; Houghton, D.D. An observation of banded convective development in the presence of weak symmetric stability. *Mon. Weather Rev.* **1988**, *116*, 175–191. [CrossRef]

39. Reuter, G.W.; Aktary, N. Convective and symmetric instabilities and their effects on precipitation: Seasonal variations in central Alberta during 1990 and 1991. *Mon. Weather Rev.* **1995**, *123*, 153–162. [CrossRef]
40. Xu, Q. Conditional symmetric instability and mesoscale rainbands. *Q. J. R. Meteorol. Soc.* **1986**, *112*, 315–334. [CrossRef]
41. Holt, M.W.; Thorpe, A.J. Localized forcing of slantwise motion at fronts. *Q. J. R. Meteorol. Soc.* **1991**, *117*, 943–963. [CrossRef]
42. Morcrette, C.J.; Browning, K.A. Formation and release of symmetric instability following Delta-M adjustment. *Q. J. R. Meteorol. Soc.* **2006**, *132*, 1073–1089. [CrossRef]
43. Fischer, C.; Lalaurette, F. Meso-β-scale circulations in realistic fronts. I: Steady basic state. *Q. J. R. Meteorol. Soc.* **1995**, *121*, 1255–1283. [CrossRef]
44. Fischer, C.; Lalaurette, F. Meso-β-scale circulations in realistic fronts. II: Frontogenetically forced basic states. *Q. J. R. Meteorol. Soc.* **1995**, *121*, 1285–1321. [CrossRef]
45. Novak, D.R.; Colle, B.A.; Yuter, S.E. High-resolution observations and model simulations of the life cycle of an intense mesoscale snowband over the northeastern United States. *Mon. Weather Rev.* **2008**, *136*, 1433–1456. [CrossRef]
46. Schultz, D.M.; Zhang, F. Baroclinic development within zonally varying flows. *Q. J. R. Meteorol. Soc.* **2007**, *133*, 1101–1112. [CrossRef]
47. Schumacher, R.S.; Schultz, D.M.; Knox, J.A. Convective snowbands downstream of the Rocky mountains in an environment with conditional, dry symmetric, and inertial instabilities. *Mon. Weather Rev.* **2010**, *138*, 4416–4438. [CrossRef]
48. Sheng, C.Y.; Yang, X.X. Symmetry instability analysis of an unusual storm snow in Shandong Province. *Meteorol. Mon.* **2003**, *28*, 33–36.
49. Zhou, X.S.; Yang, C.F.; Sun, X.C. Comparative analyses on two early spring snowstorm processes. *Plateau Meteorol.* **2013**, *32*, 446–455.
50. Skamarock, W.C.; Klemp, J.B.; Dudhia, J.; Gill, D.O.; Barker, D.M.; Duda, M.G.; Huang, X.Y.; Wang, W.; Powers, J.G. *A Description of the Advanced Research WRF Version 3. NCAR Technical Note NCAR/TN-4751STR*; National Center for Atmospheric Research: Boulder, CO, USA, 2008; 113p.
51. Chen, F.; Dudhia, J. Coupling an advanced land surface hydrology model with the Penn State–NCAR MM5 modeling system. Part I: Model description and implementation. *Mon. Weather Rev.* **2001**, *129*, 569–585. [CrossRef]
52. Kain, J.S. The Kain-Frisch convective parameterization: An update. *J. Appl. Meteorol.* **2004**, *43*, 170–181. [CrossRef]
53. Miller, J.E. On the concept of frontogenesis. *J. Meteorol.* **1948**, *5*, 169–171. [CrossRef]
54. Sawyer, J.S. The vertical circulation at meteorological fronts and its relation to frontogenesis. *Proc. R. Soc. Lond.* **1956**, *234*, 346–362.
55. Eliassen, A. On the vertical circulation in frontal zones. *Geophys. Publ.* **1962**, *24*, 147–160.
56. Hakim, G.J.; Keyser, D. Canonical frontal circulation patterns in terms of Green's functions for the Sawyer–Eliassen equation. *Q. J. R. Meteorol. Soc.* **2001**, *127*, 1795–1814. [CrossRef]
57. Thorpe, A.J.; Clough, S.A. Mesoscale dynamics of cold fronts: Structures described by dropsoundings in FRONTS 87. *Q. J. R. Meteorol. Soc.* **1991**, *117*, 903–941. [CrossRef]
58. Jurewicz, M.L.; Evans, M.S., Sr. A comparison of two banded, heavy snowstorms with very different synoptic settings. *Weather Forecast.* **2004**, *19*, 1011–1028. [CrossRef]
59. Schultz, D.M.; Knox, J.A. Banded convection caused by frontogenesis in a conditionally, symmetrically, and inertially unstable environment. *Mon. Weather Rev.* **2007**, *135*, 2095–2110. [CrossRef]
60. Chagnon, J.M.; Gray, S.L. Horizontal potential vorticity dipoles on the convective storm scale. *Q. J. R. Meteorol. Soc.* **2009**, *135*, 1392–1408. [CrossRef]
61. Blanchard, D.O.; Cotton, W.R.; Brown, J.M. Mesoscale circulation growth under conditions of weak inertial instability. *Mon. Weather Rev.* **1998**, *126*, 118–140. [CrossRef]